JOURNAL OF Materials CHEMISTRY

Synthesis and size dependent luminescent properties of hexagonal (Y,Gd)BO_3 : Eu nanocrystals

Zheng-Gui Wei, Ling-Dong Sun,* Chun-Sheng Liao, Xiao-Cheng Jiang and Chun-Hua Yan*

State Key Laboratory of Rare Earth Materials Chemistry and Applications, PKU-HKU Joint Laboratory on Rare Earth Materials and Bioinorganic Chemistry, Peking University, Beijing 100871, China. E-mail: chyan@chem.pku.edu.cn

Received 19th July 2002, Accepted 10th September 2002
First published as an Advance Article on the web 11th October 2002

Nanocrystalline (Y,Gd)BO_3 : Eu with different particle sizes have been prepared by the thermal decomposition of precursors that contain rare earths-EDTA and H_3BO_3-EDTA complexes (EDTA = ethylenediaminetetraacetate). The effects of synthesis temperature, [Y]/[Gd] value, and doping concentration of Eu^{3+} ions on the crystallization and luminescent characteristics of the (Y,Gd)BO_3 : Eu nanocrystals were investigated. The materials began to crystallize at 700 °C in air or 650 °C in oxygen with a hexagonal vaterite-type structure, except a small amount of triclinic phase evidenced at low [Y]/[Gd] value. By increasing the [Y]/[Gd] value and the calcination temperature, the triclinic phase could be eliminated. XRD patterns indicated that (Y,Gd)BO_3 : Eu nanocrystals with smaller particle size possessed a more distorted lattice, which could be responsible for the size-dependent color purity evidently showed in their photoluminescence spectra, as the ratio of the red emission ($^5D_0 \rightarrow {}^7F_2$) to the orange emission ($^5D_0 \rightarrow {}^7F_1$) (R/O) was much higher in the smaller particles. The Eu^{3+} quenching concentration and the optimum Gd^{3+} substitution also exhibited the size-dependent characteristics. Their possible mechanisms were proposed.

Introduction

Recently, vacuum ultraviolet (VUV) phosphors have been attracting much attention for their potential application in plasma display panels and Hg-free fluorescent lamps.[1,2] Rare earth orthoborates, $REBO_3$ (RE = Gd^{3+}, Y^{3+}, *etc.*), are promising candidates of desired host materials for VUV phosphors due to their high VUV transparency, exceptional optical damage threshold, and especially good VUV absorption.[3] The hexagonal vaterite-type structure of $REBO_3$ is responsible for their excellent VUV absorption.[4] However, it is obvious that a hexagonal structure has high symmetry features, and as a result, the emission of $REBO_3$: Eu is composed of almost equal contributions of $^5D_0$-$^7F_1$ and $^5D_0$-$^7F_2$ transitions, which gives rise to an orange-red emission instead of a red one and thus hampers the application of $REBO_3$: Eu. In order to increase the contributions of $^5D_0$-$^7F_2$ transition of Eu^{3+} ions and thus improve the color purity, lowering the system symmetry of $REBO_3$ is required. However, at the same time, one must not change the hexagonal vaterite-type structure of $REBO_3$: Eu so as to keep their high VUV efficiency. Our previous work realized this design in nano-sized YBO_3 : Eu, which maintained vaterite-type structure and possessed lower symmetry simultaneously.[5] In fact, YBO_3 : Eu is not the best performing VUV phosphor. Its VUV luminescent efficiency is about 20% lower than that of (Y,Gd)BO_3 : Eu, for that Gd^{3+} might play an important role in the energy transfer process of VUV phosphors.[6,7] This work will focus on the synthesis and size-dependent luminescent properties of hexagonal (Y,Gd)BO_3 : Eu nanocrystals.

It is well known that $REBO_3$ is apt to form highly agglomerated particles. Therefore, although numerous bulk $REBO_3$: Eu fabrication techniques can be easily found, such as solid-state reaction,[3,6] co-precipitation,[8] microwave heating,[9] spray pyrolysis,[7] and sol-gel method,[8] *etc.*, only a few reports were presented on the synthesis of $REBO_3$: Eu nanocrystals. Recently, Lou *et al.* prepared 40 ~ 60 nm YBO_3 : Eu waveguide film through a sol-gel route,[10] starting from the preparation of boron yttrium and boron europium hetero-metallic alkoxides within a system with a controlled humidity. Zhang *et al.* synthesized 40 nm YBO_3 : Eu nanocrystals using a sol-gel method, where it is difficult to obtain a pure hexagonal phase nanosized YBO_3 : Eu at a low calcination temperature (below 800 °C).[11] In this investigation, we synthesized (Y,Gd)BO_3 : Eu nanocrystals by the thermal decomposition of precursors (***TP***) that contained RE-EDTA and H_3BO_3-EDTA complexes (EDTA = ethylenediaminetetraacetate). The salient advantage of this route is that hexagonal phased (Y,Gd)BO_3 : Eu with high luminescent intensity and superior color purity can be obtained at a low annealing temperature.

Experimental

The starting materials used for the preparation of (Y,Gd)BO_3 : Eu nanocrystals were H_3BO_3, $(NH_4)_2$-EDTA, Y_2O_3, Gd_2O_3 and Eu_2O_3. The synthesis is as follows. Appropriate amounts of RE_2O_3 were dissolved in dilute HNO_3, then boric acid and $(NH_4)_2$-EDTA were quantitatively added to this solution at a molar ratio of EDTA : RE : H_3BO_3 = 2.03 : 1 : 1.03, and then it was kept stirring until a homogenous solution was formed. Here, 3% excess amount of boric acid was used to compensate for its evaporation loss. The pH of the solution was finally controlled to 6 ~ 7. By slowly evaporating the solvent, the precursors were obtained and then were dried at 80 °C under a vacuum for 10 hours. Elemental analysis (%): found C, 21.03; H, 5.29; N, 16.38; Calc. C, 20.91; H, 5.43; N, 17.00 for the precursor complex mixture $C_{20.3}H_{62.78}N_{14.15}O_{33.36}B_{1.03}$ [NH_4-EDTA-RE·$4H_2O$ and $3NH_4NO_3$ and 1.03 ($(NH_4)_3$-EDTA-$B(OH)_2 \cdot 2H_2O$)]. TG-DTA analysis, weight loss percentage and corresponding thermal effect: 21.46% [110–266 °C, very strong endothermic], 34.54% [266–439 °C, weak exothermic], 17.73% [439–540 °C, very strong exothermic].

Since the H_3BO_3-EDTA complex, which may have similar

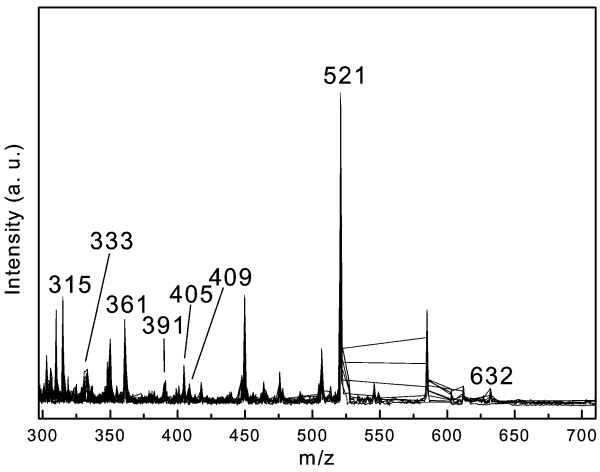

Fig. 1 FAB-MS of the H_3BO_3-EDTA complex.

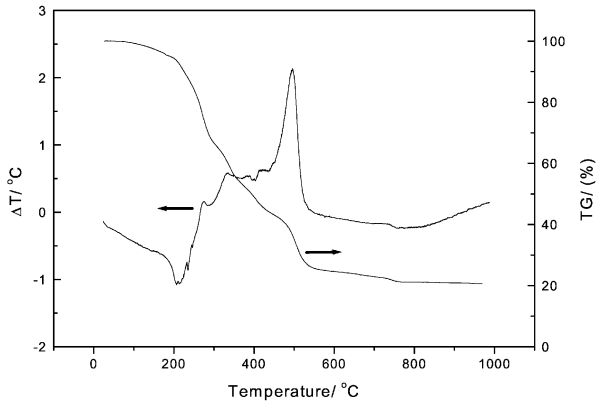

Fig. 2 Combined TG-DTA curves of the precursor complex mixture.

coordination behaviors to yttrium and europium EDTA complexes, might be responsible for the avoidance of aggregation, it was also prepared for further analysis. The synthetic procedure is the same as the one described above, except that only boric acid and $(NH_4)_2$-EDTA were employed as starting materials.

Aliquots of the precursor were calcined at 650 °C for 5 h in oxygen, at 900 °C for 5 h in air to obtain nanosized samples, and at 1100 °C for 5 h in air to obtain submicronsized $(Y,Gd)BO_3:Eu$. These samples are denoted successively as ***TP1***-, ***TP2***-, and ***TP3***-series, respectively, in the following description. For comparison, the bulk $(Y,Gd)BO_3:Eu$ was obtained by direct solid-state reaction (***SR***) from the mixture of Y_2O_3, Gd_2O_3, Eu_2O_3 and H_3BO_3 at 1100 °C for 10 h in air.

Dense pellet samples with diameters of 10 mm were obtained under a press of 6 MPa. Au coating was sputtered onto the surface of these dense pellet samples for recording the micrographs.

X-ray Diffraction (XRD) studies were carried out on a Rigaku D/max-2000 X-ray powder diffractometer using Cu K_α (λ = 1.5405 Å) radiation. SEM images were taken on an Amary 1910 field emission scanning electron microscope. Elemental analysis of C, H and N was performed with a Carlo Erba 1102 element analyzer and TG-DTA was investigated by using a Du Pont 2100 thermal analyzer in air. Mass spectrum of H_3BO_3-EDTA complex was recorded on a ZAB-HS model FABMS spectrometer (VG Co. Ltd., UK). Fluorescence spectra were determined on a Hitachi F-4500 spectrophotometer at room temperature.

Results and discussion

1 Thermal decomposition behavior of the complex precursor

Previously, it was neglected that boric acid can form complex by reacting with the molecules which have two or more carboxyl (or hydroxyl) groups,[12] and to our knowledge, no one has yet utilized H_3BO_3-EDTA complex as a precursor to synthesize nanosized borate materials. In this paper, we characterized H_3BO_3-EDTA by FABMS, and the result is shown in Figure 1. The main peaks of the spectra are located at 315, 333, 361, 391, 405, 409, 521 and 632, which can be assigned to be $(EDTA\text{-}BO)^{3-}$, $(EDTA\text{-}B(OH)_2)^{3-}$, $((OH)_2B\text{-}EDTA\text{-}B(OH)_2H)^{-}$, $H_2EDTA\text{-}B_3O_4H$, $(EDTA\text{-}B_3O_5H)^{4-}$, $H_2EDTA\text{-}B_3O_5H_3$, $(B_3O_5\text{-}EDTA\text{-}B_3O_5H)^{5-}$, and $(BO_2H\text{-}EDTA\text{-}B\text{-}EDTA)^{4-}$ respectively. The spectrum is complicated, but it is of no doubt that H_3BO_3-EDTA complex is formed.

The TG-DTA curves of the complex precursor were studied and displayed in Figure 2 to understand its pyrolysis behavior. The decomposition process can be roughly divided into two periods. The first corresponds to a very strong endothermic peak below 270 °C, which is caused by the release of H_2O. The second is associated with a weak exothermic peak at 266–439 °C and a very strong exothermic peak at 439–540 °C, which originate from the burning of the EDTA ligand. All organic matters are burnt out above 540 °C, and there is almost no weight loss thereafter.

For the further investigation of the residual burnt organic impurities, elemental analysis was carried out for as-prepared $(Y,Gd)BO_3:Eu$ (Table 2). The amount of impurities decreased with increasing calcination temperature, and the impurities were almost completely removed (below 1%) beyond 900 °C in air. The time dependence of impurity content for calcination at 650 °C in oxygen is also listed in Table 1. The results showed that the increase of calcination time was of benefit to eliminating the organic contaminants. The content of the remnant impurities became very little (below 1%) after 5 h calcination at 650 °C in oxygen, indicating that the calcination at a relatively low temperature can also lead to a pure material, but then the oxygen atmosphere and enough long calcination time are necessary. It should be mentioned that the [Y]/[Gd] value influences the amount of the impurities to a much less degree in comparison with the calcination temperature and time, as is shown in Table 1.

Table 1 Elemental analysis results of some impurities in the calcinated $(Y_{0.9-y}Gd_y)BO_3:Eu_{0.1}$ nanocrystals

Temperature/°C (in air, 5 h, y = 0.30)	C (%)	H (%)	N (%)	Time/h (at 650 °C in oxygen, y = 0.30)	C (%)	H (%)	N (%)
550	3.915	0.348	3.250	0.67	3.670	0.395	2.909
650	1.474	0.220	0.890	1.67	1.051	0.253	0.985
900	0.230	0.026	0.155	3	0.620	0.105	0.743
1100	0.199	0.041	0.105	5	0.431	0.076	0.448
y (at 900 °C, 5 h, in air)	C (%)	H (%)	N (%)	y (at 650 °C, 5 h, in oxygen)	C (%)	H (%)	N (%)
0	0.272	0.031	0.090	0	0.443	0.086	0.503
0.9	0.277	0.029	0.190	0.9	0.573	0.104	0.222

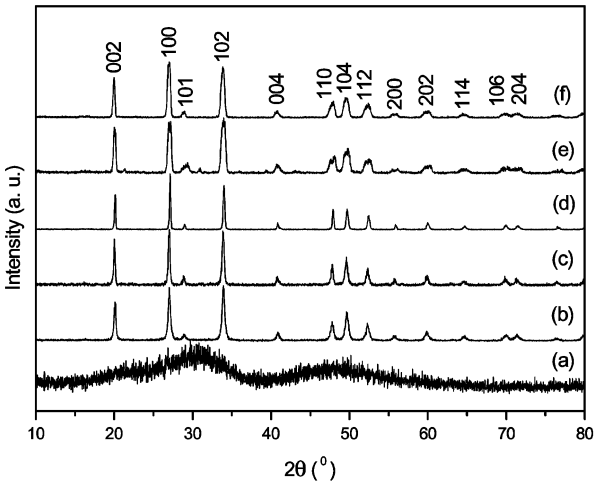

Fig. 3 XRD patterns of $(Y_{0.6}Gd_{0.3})BO_3:Eu_{0.1}$ samples. Complex precursors are decomposed at 550 °C (**a**) in air, 650 °C (**b**, denoted as ***TP1*** in the text and following figures) in oxygen, 900 °C (**c**, ***TP2***) and 1100 °C (**d**, ***TP3***) in air for 5 h, respectively. Bulk sample is obtained by direct solid-state reaction at 1100 °C for 5 h (**e**), and 10 h (**f**, ***SR***).

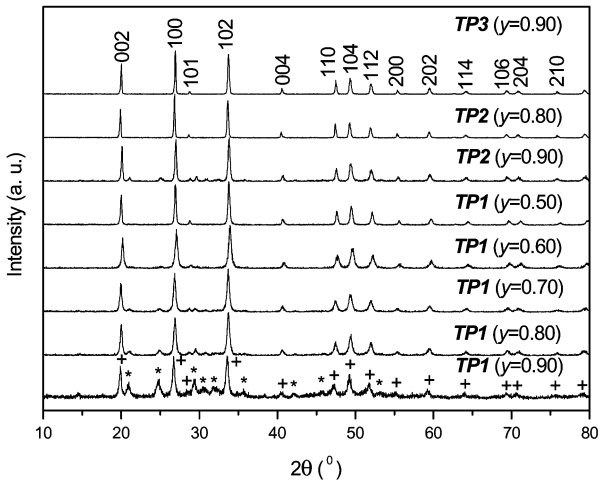

Fig. 4 XRD patterns of $(Y_{0.9-y}Gd_y)BO_3:Eu_{0.1}$ samples. "+" and "*" label the hexagonal and triclinic phases, respectively.

2 Microstructure characterization of (Y,Gd)BO_3 : Eu nanocrystals

Figure 3(a–d) shows the XRD patterns for $(Y_{0.6}Gd_{0.3})BO_3:Eu_{0.1}$ samples formed by the ***TP*** process. The crystallization of (Y,Gd)BO_3 : Eu took place at 650 °C in oxygen and at 700 °C in air. All the XRD peaks of (Y,Gd)BO_3 : Eu samples obtained beyond these temperatures could be indexed to the hexagonal phase of YBO_3 with vaterite-type structure, and no excessive traces of rare earth oxide were observed, suggesting that the ***TP*** process allowed a low sintering temperature. For comparison, figure 3(e,f) presents the bulk $(Y_{0.6}Gd_{0.3})BO_3:Eu_{0.1}$ phosphors prepared by ***SR*** at 1100 °C for 5 h and 10 h, respectively. Each diffraction direction consists of at least two peaks in figure 3(e), indicating that the ***SR*** sample heated below 5 h was only a mixture of hexagonal YBO_3, $EuBO_3$, and $GdBO_3$. The multiple peaks degenerated into a single peak in each diffraction while the ***SR*** sample was heated over 10 h, demonstrating that only at the calcination time beyond 10 h could the (Y,Gd)BO_3 : Eu solid solution be formed. The ***SR*** samples possessed broader XRD lines in comparison with ***TP3***, suggesting the inferior homogeneity in the ***SR*** samples. This broadening could not be ascribed to the particle-size decrease, since SEM photographs will reveal that the particle size of the ***SR*** samples is in fact larger than that of ***TP3***.

Figure 4 displays the influence of Gd^{3+} concentration on the XRD patterns for *TP* samples. For ***TP1*** samples, which were prepared at 650 °C, only when the y values in $(Y_{0.9-y}Gd_y)BO_3:Eu_{0.1}$ were lower than or equal to 0.5 could they adopt a pure hexagonal form. When y values were higher than 0.5, a small amount of triclinic appeared, and the proportion of triclinic impurity increased with the Gd^{3+} concentration. However, for ***TP2*** samples, which were synthesized at 900 °C, the limit of y values changed, and as long as y was lower than or equal to 0.8, the triclinic phase ceased to appear. For ***TP3*** sample prepared at 1100 °C, we did not find any triclinic phase even when Y^{3+} was totally substituted by Gd^{3+}. Since the triclinic impurity could be eliminated by increasing temperature or decreaseing the proportion of Gd^{3+}, we could safely conclude that the triclinic phase was the stabler structure of $GdBO_3$ at low temperature. The following studies were focused on the (Y,Gd)BO_3 : Eu samples with pure hexagonal phase only when y is lower than 0.5.

By applying Scherrer formula[13] to the full width at half maximum of the diffraction peaks, the average particle size of $(Y_{0.6}Gd_{0.3})BO_3:Eu_{0.1}$ could be calculated as 32.4 and 90.2 nm for ***TP1*** and ***TP2*** samples, respectively. Obviously, the sizes of (Y,Gd)BO_3 : Eu samples increased with annealing temperature and time.

The least-squares refined crystallographic unit cell parameters were obtained by using the software "LAPOD",[14] as listed in Table 2. With decreasing the particle size, a values increased throughout, while the increasent trend of c values could only be observed in the samples with relatively large particle sizes, which resulted in an increscent trend of cell volume values and a decrescent trend of c/a values. The variation of a values was not identical to that of c values, indicating that the particle-size decrease resulted in a distortion of (Y,Gd)BO_3 : Eu lattices. The c/a value can be taken as the measure of the lattice distortion. Results revealed that the lattices are more distorted in the nanocrystals than in the bulk, and the smaller the particle size, the more distorted the lattices. For ***TP2*** samples, the decrease of the [Y]/[Gd] value led to the increase of the cell parameters. However, unlike the decrescent trend of c/a values observed as the particle size decreased, the c/a values of all ***TP2*** samples were almost equal to each other

Table 2 Least squares refined unit cell parameters for $Y_{0.9-y}Gd_yBO_3:Eu_{0.1}$ bulk and nanocrysatlline samples

sample	a (Å)	c (Å)	c/a	cell volume (Å^3)
bulk (y = 0.3)	3.7882 ± 0.0008	8.8181 ± 0.0021	2.3278 ± 0.0008	109.59 ± 0.044
TP3 (y = 0.3)	3.7932 ± 0.0014	8.8306 ± 0.0036	2.3280 ± 0.0013	110.03 ± 0.076
TP2 (y = 0.3)	3.8051 ± 0.0013	8.8424 ± 0.0032	2.3238 ± 0.0012	110.88 ± 0.068
TP1 (y = 0.3)	3.8103 ± 0.0009	8.8367 ± 0.0023	2.3192 ± 0.0008	111.11 ± 0.050
TP2 (y = 0.1)	3.8044 ± 0.0014	8.8383 ± 0.0035	2.3256 ± 0.0013	110.55 ± 0.075
TP2 (y = 0.2)	3.8028 ± 0.0019	8.8457 ± 0.0046	2.3261 ± 0.0017	110.78 ± 0.098
TP2 (y = 0.4)	3.8107 ± 0.0006	8.8583 ± 0.0016	2.3246 ± 0.0006	111.40 ± 0.034
TP2 (y = 0.5)	3.8215 ± 0.0015	8.8901 ± 0.0381	2.3263 ± 0.0136	112.44 ± 0.815

Complex precursors are decomposed at 650 °C (***TP1***), 900 °C (***TP2***), and 1100 °C (***TP3***) for 5 h, respectively. Bulk sample is obtained by direct solid-state reaction at 1100 °C for 5 h.

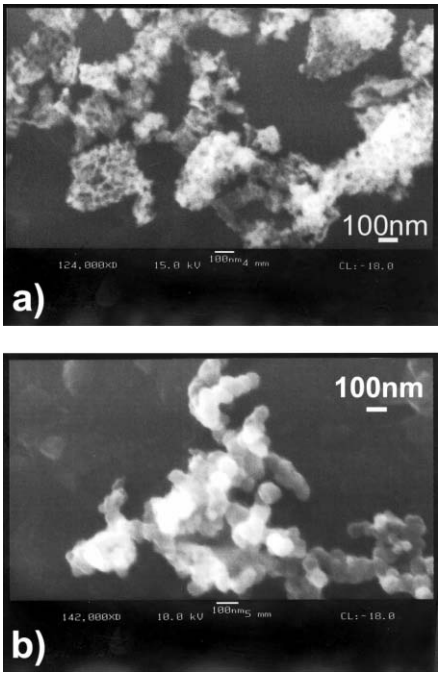

Fig. 5 SEM images of $(Y_{0.6}Gd_{0.3})BO_3:Eu_{0.1}$ for (**a**) ***TP1*** and (**b**) ***TP2***.

and were around 2.325, indicating that the lattices of all ***TP2*** samples were distorted at the same degree for their similar particle size. It can be concluded that the lattice distortion of $(Y,Gd)BO_3:Eu$ nanocrystals is dependent on the particle size, whereas independent of the [Y]/[Gd] value.

Previous studies showed that in addition to the limited coherence length of the nanocrystals, many bulk and surface defects existed as a consequence of the low temperature synthesis and the high surface area of the crystallites.[15] These defects may account for the lattice distortion in the nanocrystals.

The SEM images of $(Y_{0.6}Gd_{0.3})BO_3:Eu_{0.1}$ samples are shown in Figure 5. It revealed that the primary particles of the nanosized $(Y,Gd)BO_3:Eu$ powders were sphere-like in configuration. These primary particles are approximately 30 and 90 nm for ***TP1*** and ***TP2***, respectively, which is consistent with the results obtained from XRD. These primary particles were loosely clustered into agglomerates up to micron level.

Figure 6 exhibits the SEM photographs of the dense pellet specimens at different magnification. The specimens were composed of a large number of small grains. The sizes of these grains were about 90, 500, and 1000 nm for ***TP2***, ***TP3***, and ***SR***, respectively, which were consistent with the above results deduced from XRD data. Moreover, the ***TP*** samples possessed higher densification and smoother surface in comparison with the ***SR*** sample, which may explain the luminescent yield improvement in ***TP*** samples, as mentioned in the next section.

3 Size dependent luminescent properties in $(Y,Gd)BO_3:Eu$ nanocrystals

Figure 7 displays the emission spectra of $(Y_{0.6}Gd_{0.3})BO_3:Eu_{0.1}$ under 240 nm UV irradiation. The spectra consist of sharp lines ranging from 580 to 720 nm, which are associated with the

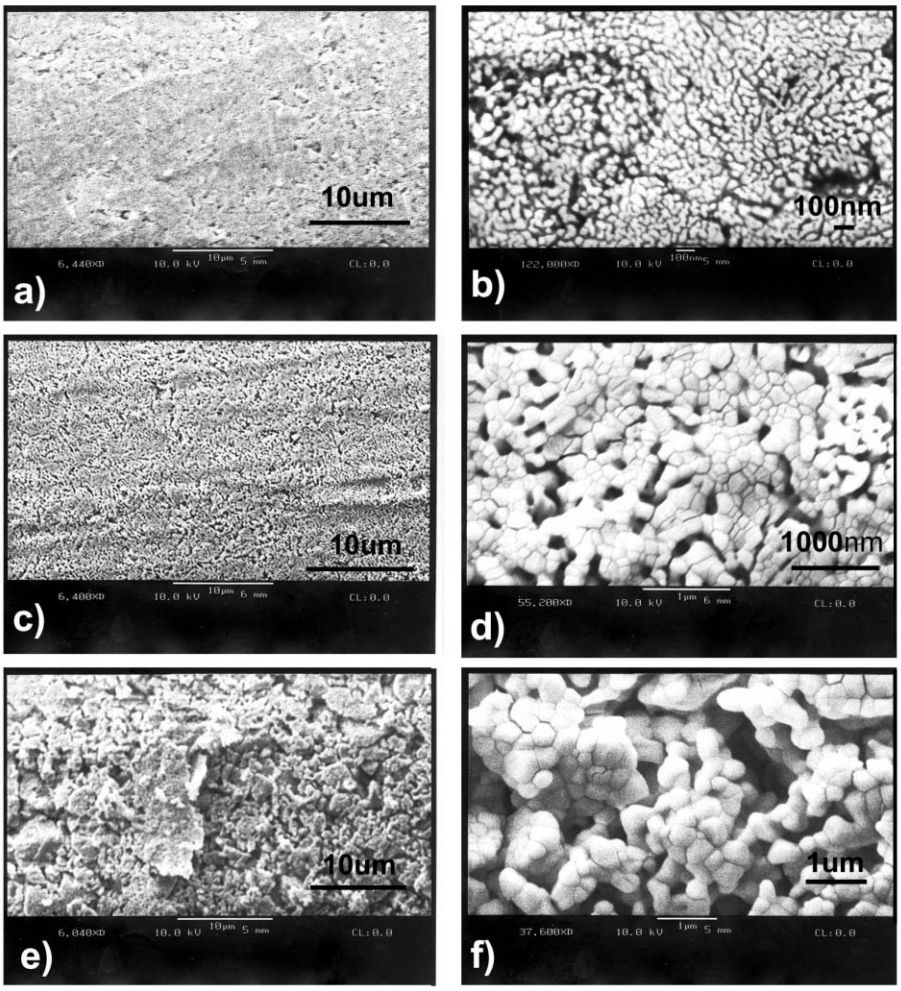

Fig. 6 SEM images of $(Y_{0.6}Gd_{0.3})BO_3:Eu_{0.1}$ for (**a**) ***TP2*** at 6440 × magnification, (**b**) ***TP2*** at 122000 × magnification, (**c**) ***TP3*** at 6400 × magnification, (**d**) ***TP3*** at 55200 × magnification, (**e**) ***SR*** at 6040 × magnification, (**f**) ***SR*** at 37600 × magnification.

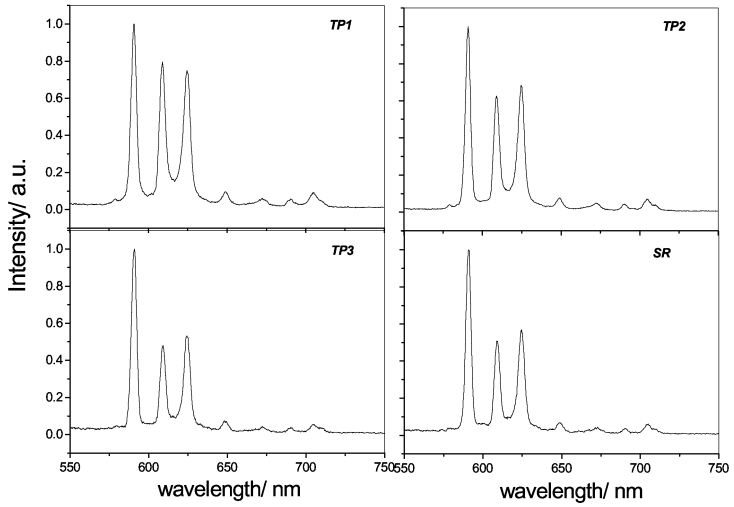

Fig. 7 Emission spectra of $(Y_{0.6}Gd_{0.3})BO_3:Eu_{0.1}$ for samples ***TP1***, ***TP2***, ***TP3***, and ***SR***.

transitions from the excited $^5D_0$ level to ^7F_J (J = 1, 2, 3, 4) levels of Eu^{3+} activators.[16,17] The major emissions of (Y,Gd)BO_3 : Eu are at 591 nm ($^5D_0$-$^7F_1$) and 610, 625 nm ($^5D_0$-$^7F_2$), which correspond to orange-red and red color, respectively. The luminescent intensity of (Y,Gd)BO3 : Eu increases with increasing the decomposition temperature, and the highest intensity is obtained in sample ***TP3***, which is about twice as high as that of the bulk (Y,Gd)BO_3 : Eu. Boyer *et al.* considered that the luminescent efficiency of polycrystalline YBO_3 : Eu was correlated with the synthesis routes, and the YBO_3 : Eu synthesized from sol-gel process appeared to have a higher efficiency than that synthesized from solid state reaction and wet process.[8] Similarly, the Y_2O_3 : Eu nanocrystals with the particle sizes of about 70 nm synthesized by combustion,[18] sol-gel process[19] and heating the amorphous precursor[20] have the luminescent efficiency which is 10, 30 and 110–120% of that of the bulk Y_2O_3 : Eu, respectively. Our work coincides with these results. Moreover, although the major peak positions are identical to each other, the intensity patterns are quite different. For the bulk and submicronsized samples, the $^5D_0$-$^7F_1$ transition is by far the most intense.[6,7] But the relative intensity of $^5D_0$-$^7F_2$ increases with decreasing particle size. It is obvious that as the particle size decreases, the red emission coming from $^5D_0$-$^7F_2$ increases, and as a result, a better color purity, *i.e.*, a redder fluorescence, in chromatic sense, can be obtained from the smaller sized (Y,Gd)BO_3 : Eu.

The intensity of transitions between different J levels depends on the symmetry of the local environment of the Eu^{3+} activators and can be described in terms of Judd-Ofelt theory.[17] Magnetic dipole transition is permitted and electric dipole transition is forbidden. But for most cases, the local symmetry of the Eu^{3+} activators does not have an inversion center and the parity forbidden is partially permitted, such as Eu^{3+} ions occupying C_2 sites in Y_2O_3 : Eu.[17] It is well known that the relative intensity of $^5D_0$-$^7F_1$ transition (a typical magnetic dipole transition) or $^5D_0$-$^7F_2$ transition (a typical electric dipole transition) depends strongly on the local symmetry of Eu^{3+} ions. Subsequently, when Eu^{3+} ions occupy the inversion center sites, the $^5D_0$-$^7F_1$ transition will be relatively strong, while the $^5D_0$-$^7F_2$ transition is parity forbidden and will be very weak. The abnormal luminescent behavior of the nanosized (Y,Gd)BO_3 : Eu must be correlated with the microstructure of the nanoparticles. As is mentioned above, numerous surface defects exist as a consequence of the low temperature synthesis and the high surface area of the crystallites. These defects may raise the degree of disorder and thus lower the local symmetry of Eu^{3+} ions. This will increase the transition probability of $^5D_0$-$^7F_2$ and enhance the red emission visually although the luminescent spectra are still the mixture of orange-red and red emission bands in the nanosized (Y,Gd)BO_3 : Eu.

The relationship between luminescent intensity of $^5D_0$-$^7F_2$ and Eu^{3+} dopant content is shown in Figure 8. The quenching concentration varies with the particle size. It is about 8% for the bulk (Y,Gd)BO_3 : Eu and increases to 10, 15 and 20% for submicronsized sample, 90.2 and 32.4 nm (Y,Gd)BO_3 : Eu nanoparticles, respectively. The deficiency of the traps due to the limited primitive cells per particle, as well as the hindrance of energy transfer by the particle boundary is responsible for the size dependence of quenching concentration.[5,15,21] It should be mentioned that higher quenching concentration does not mean stronger luminescence, just as what was observed in smaller particles.[5,22]

Figure 9 exhibits the change of emitting intensity with Gd^{3+} concentration in $Y_{0.9-y}Gd_yBO_3:Eu_{0.1}$ phosphors. The optimum Gd^{3+} concentration was found to be 30, 30, 25 and 20% for the bulk, submicronsized, 90.2 and 32.4 nm (Y,Gd)BO_3 : Eu, respectively. This is the result of the balance between the two effects of the Gd^{3+} substitution on the system. With Gd^{3+} substitution, the energy transfer from Gd^{3+} to Eu^{3+} activator will lead to increased emission intensity.[6,7] However, at the same time, the lengthening of RE-O distance, which results from the relatively larger ion radius of Gd^{3+}, will lead to a lower luminescent yield.[18] The former factor might dominate at low Gd^{3+} substitution, while the latter might dominate at the

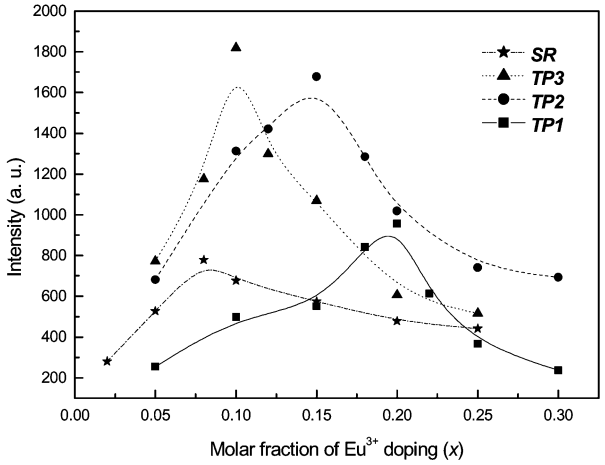

Fig. 8 The emission intensity of $^5D_0$-$^7F_2$ in relation to Eu^{3+} doping concentration for $(Y_{0.67-0.67x}Gd_{0.33-0.33x})BO_3:Eu_x$ samples.

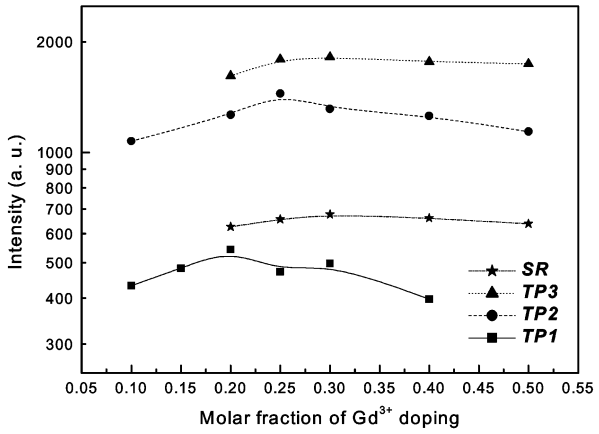

Fig. 9 The effect of Gd^{3+} substitution on the emission intensity of $^5D_0$-$^7F_2$ for $(Y_{0.9-y}Gd_y)BO_3:Eu_{0.1}$ samples.

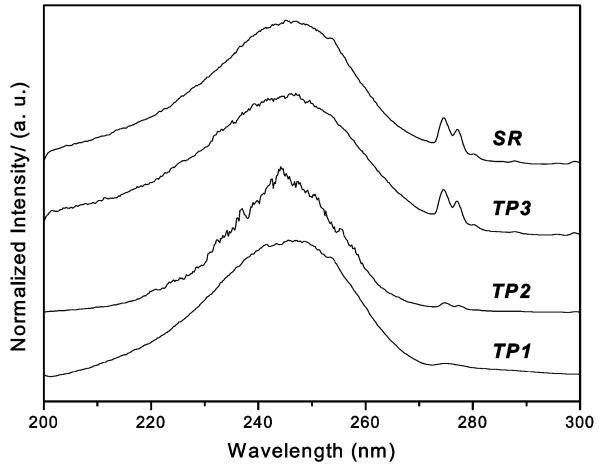

Fig. 10 Excitation spectra of $(Y_{0.6}Gd_{0.3})BO_3:Eu_{0.1}$ for samples ***TP1***, ***TP2***, ***TP3***, and ***SR*** obtained by monitoring the emissions of $^5D_0 \rightarrow {}^7F_2$ (at 610 nm).

high Gd^{3+} substitution, and as a result, an optimum Gd^{3+} substitution could be observed.

Figure 10 is the excitation spectra of $^5D_0$-$^7F_2$ emission of Eu^{3+} ions for various phosphors. The intense broad band at 245 nm corresponded to the charge transfer (CT) of Eu^{3+} ions. It is well known that through CT process, the Eu^{3+} ions are directly promoted from the ground state to the excited state. The peaks at 274 and 277 nm were associated with the energy transfer from Gd^{3+} to Eu^{3+} activator, which could be realized by two different processes, one excitation process of the Gd^{3+} ions and one energy transfer process from Gd^{3+} to Eu^{3+}. When the particle size became smaller, the surface defects would multiply, and more Gd^{3+} in the excited state would be deexcited by transferring energy to surface defects. Therefore, the energy transfer process from Gd^{3+} to Eu^{3+} possessed an additional probability of nonradiative transition comparing to the CT process, and as a result, a relative decrease of the peaks at 274 and 277 nm could be observed in the smaller sized $(Y,Gd)BO_3:Eu$. This could explain the lower optimum Gd^{3+} substitution in smaller sized $(Y,Gd)BO_3:Eu$, which has a weaker energy transfer efficiency from Gd^{3+} to Eu^{3+} due to the higher probability of nonradiative transition.

Conclusion

In this work, a convenient alternative route, thermal decomposition technology, was applied in the fabrication of hexagonal $(Y,Gd)BO_3:Eu$ nanocrystals, and H_3BO_3-EDTA complex, a new precursor for nanosized borate materials, was proposed for the first time. As the crystallization and luminescent characteristics can be greatly affected by the experimental conditions, we have carefully investigated the effect of preparation temperature, [Y]/[Gd] value, and doping concentration of Eu ions and presented some possible explanations. Under the optimum conditions, a pure hexagonal vaterite-type phased $(Y,Gd)BO_3:Eu$ nanocrystals could be obtained at a relatively low temperature and the fluorescence intensity as well as the color purity were significantly improved, all of which are critical to the application of the VUV phosphors and our comprehension on the mechanisms of the emission process.

Acknowledgements

This work is supported by the NSFC (20001002, 20013005), MOST (G19980613), MOE (the Foundation for University Key Teacher), and the Founder Foundation of PKU.

References

1 C. R. Ronda, T. Jüstel and H. Nikol, *J. Alloy Compd.*, 1998, **275–277**, 669.
2 C.-H. Kim, I.-E. Kwon, C.-H. Park, Y.-J. Hwang, H.-S. Bae, B.-Y. Yu, C.-H. Pyun and G.-Y. Hong, *J. Alloys Compd.*, 2000, **311**, 33.
3 M. Ren, J. H. Lin, Y. Dong, L. Q. Yang, M. Z. Su and L. P. You, *Chem. Mater.*, 1999, **11**, 1576.
4 Z. Yang, M. Ren, J. H. Lin, M. Z. Su, Y. Tao and W. Wang, *Chem. J. Chinese U.*, 2000, **21**, 1339.
5 Z. G. Wei, L. D. Sun, C. S. Liao, C. H. Yan and S. H. Huang, *Appl. Phys. Lett.*, 2002, **80**, 1447.
6 X. Y. Wu, G. Y. Hong, X. Q. Zeng, H. P. You, C. H. Kim, C. H. Pyun, H. S. Bal, B. Y. Yu, I. E. Kwon and C. H. Park, *Chem. J. Chinese U.*, 2000, **21**, 1658.
7 D. S. Kim and R. Y. Lee, *J. Mater. Sci.*, 2000, **35**, 4777.
8 D. Boyer, G. Bertrand-Chadeyron, R. Mahiou, C. Caperaa and J. C. Cousseins, *J. Mater. Chem.*, 1999, **9**, 211.
9 Y. Y. Li, M. L. Peng and S. H. Feng, *Chinese Chem. Lett.*, 1996, **7**, 387.
10 L. Lou, D. Boyer, G. Bertrand-Chadeyron, E. Bernstein, R. Mahiou and J. Mugnier, *Opt. Mater.*, 2000, **15**, 1.
11 W. W. Zhang, P. B. Xie, W. P. Zhang, M. Yin, L. Jing, S. Z. Lü, L. R. Lou and S. D. Xia, *J. Inorg. Mater.*, 2001, **16**, 9.
12 K. Kustin and R. Pizer, *J. Am. Chem. Soc.*, 1969, **91**, 317.
13 Y. W. Zhang, J. T. Jia, C. S. Liao and C. H. Yan, *J. Mater. Chem.*, 2000, **10**, 2137.
14 J. I. Langford, *J. Appl. Cryst.*, 1973, **6**, 190.
15 A. Huignard, T. Gacoin and J. P. Pierre, *Chem. Mater.*, 2000, **12**, 1090.
16 K. Riwotzki and M. Haase, *J. Phys. Chem.B*, 1998, **102**, 10129.
17 R. Reisfeld and C. K. Jφrgensen, *Lasers and Excited States of Rare Earths*; Springer-Verlag: Berlin Heidelberg, 1977.
18 Y. Tao, G. W. Zhao, X. Ju, X. G. Shao, W. P. Zhang and S. D. Xia, *Mater. Lett.*, 1996, **28**, 137.
19 J. Dhanaraj, R. Jagannathan, T. R. N. Kutty and C. H. Lu, *J. Phys. Chem.B*, 2001, **105**, 11098.
20 G. Wakefield, E. Holland, P. J. Dobson and J. L. Hutchison, *Adv. Mater.*, 2001, **13**, 1557.
21 W. P. Zhang, P. B. Xie, C. K. Duan, K. Yan, M. Yin, L. R. Lou, S. D. Xia and J. C. Krupa, *Chem. Phys. Lett.*, 1998, **292**, 133.
22 B. M. Tissue, *Chem. Mater.*, 1998, **10**, 2837.